THE JOURNAL OF PHYSICAL CHEMISTRY C

Article

pubs.acs.org/JPCC

Effects of the Incorporation of Sc_2O_3 into CeO_2–ZrO_2 Solid Solution: Structural Characterization and in Situ XANES/TPR Study under H_2 Atmosphere

Lucía M. Toscani,[†] Aldo F. Craievich,[‡] Márcia C. A. Fantini,[‡] Diego G. Lamas,[§,⊥] and Susana A. Larrondo*[,†,∥]

[†]UNIDEF, MINDEF, CONICET, Departamento de Investigaciones en Sólidos, CITEDEF, J.B. de La Salle 4397, 1603 Villa Martelli, Pcia. de Buenos Aires, Argentina

[‡]Instituto de Física, Universidade de São Paulo, Rua do Matão 1371, 05508-090 São Paulo, SP, Brazil

[§]CONICET y Escuela de Ciencia y Tecnología and [∥]Instituto de Investigación e Ingeniería Ambiental, UNSAM, Campus Miguelete, 25 de Mayo y Francia, 1650 San Martín, Pcia. de Buenos Aires, Argentina

[⊥]Departamento de Física de la Materia Condensada, Gerencia de Investigación y Aplicaciones, Centro Atómico Constituyentes, Comisión Nacional de Energía Atómica, Av. General Paz 1499, 1650 San Martín, Pcia. de Buenos Aires, Argentina

ABSTRACT: Nanostructured CeO_2-rich samples cosubstituted with ZrO_2 and Sc_2O_3 are studied. The effects of the combined additions of both oxides on structural, morphological, and, especially, redox properties of the substituted lattice are assessed. In situ near edge X-ray absorption (XANES) experiments with synchrotron light were performed to study oxygen exchange capacity in a reducing environment for these ternary oxides. Structural characterization revealed that up to 8 at. % Sc was successfully incorporated into the CeO_2–ZrO_2 lattice without phase segregation. Increased scandia solubility was achieved through a soft chemical route synthesis involving citrate complexation which gave rise to porous powders with crystallite sizes in the nanometer range. In situ XANES experiments in 5 mol % H_2/He atmosphere demonstrated that adding Sc^{3+} to the CeO_2–ZrO_2 mixed oxide leads to a ternary system ($Ce_{0.9}Sc_xZr_{0.1-x}O_{2-\delta}$) with faster reduction kinetics and enhanced reducibility in the whole temperature range analyzed (25–800 °C) compared to both binary materials: $Ce_{0.9}Zr_{0.1}O_2$ and $Ce_{0.9}Sc_{0.1}O_{1.95}$.

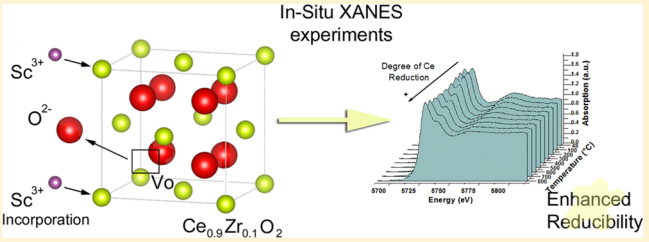

1. INTRODUCTION

Ceria-based materials have been widely studied in the past decades due to their interesting defect chemistry and enhanced redox capability that enabled their use in an extensive variety of applications such as catalysis and electrochemistry.[1] Pure CeO_2 presents a fluorite-type cubic crystalline structure ($Fm\bar{3}m$ space group) with high oxygen mobility in the lattice due to the reversible interplay of Ce^{4+}/Ce^{3+} species in oxidizing and reducing atmospheres. The reduction of Ce^{4+} to Ce^{3+} gives rise to the formation of oxygen vacancies to compensate charge fluctuations. As a result, the presence of oxygen vacancies enables oxygen diffusivity through a vacancy hopping mechanism in the anion sublattice of the fluorite structure.[2]

Oxygen diffusivity in ceria-based materials is highly required, in particular in the field of intermediate temperature solid-oxide fuel cells (IT-SOFCs), where materials with mixed ionic and electronic conductivity are sought after.[3] SOFC anode materials need to be able to oxidize the fuel molecule with the O^{2-} ions incoming from the electrolyte. In this sense, these materials should guarantee access to the gas-phase fuel molecule through the structure to reach the oxygen ions. Therefore, a porous structure is highly desirable.

In fact, if high ionic conduction takes place in the anode, the reaction is not confined to the triple phase boundary (TPB), but instead it occurs within the whole surface area where the oxygen ions surpassing the anode–electrolyte interface are located. Furthermore, if hydrocarbons are used as fuels, oxygen mobility in the lattice can promote gasification of carbon species deposited in the material surface.[4]

The effects of rare-earth (RE) and transition metal (TM) additions to ceria have been extensively studied in order to tailor its properties, making it suitable for specific applications.[5,6] In particular, in the area of catalysis, the addition of ZrO_2 to the CeO_2 lattice has proven to enhance redox properties and catalytic activity for hydrocarbon oxidation and to favor thermal stability by preventing particle sintering and consequent loss of surface area at high temperatures.[7−10]

On the other hand, the effects of aliovalent addition to ceria have been thoroughly investigated in light of increasing its ionic conductivity by promoting the formation of oxygen vacancies,[11−13] especially for IT-SOFC electrolyte and electrode

Received: August 3, 2016
Revised: September 28, 2016
Published: October 4, 2016

DOI: 10.1021/acs.jpcc.6b07847
J. Phys. Chem. C 2016, 120, 24165−24175

applications.[3] For low oxygen vacancy content its increase promotes the increase of ionic conductivity. However, this effect reaches a maximum after which the formation of additional oxygen vacancies leads to a drop in conductivity. This feature has been assigned to the increasing effect of defect−defect interactions.[12−14]

The material with composition $Ce_{0.9}Zr_{0.1}O_2$ has excellent redox and catalytic properties and exhibits morphological and phase stability in the IT-SOFC regime.[5,15,16] However, the addition of a lower valence cation to this system is expected to allow for the incorporation of additional defects.

In order to establish the effects of the addition of trivalent RE to CeO_2, the system $CeO_2-Sc_2O_3$ (0.05−3 mol % Sc-substituted Ce) has been studied by Gerhardt et al.[11] These authors compared the ionic conductivities obtained for the studied $CeO_2-Sc_2O_3$ system with those corresponding to other RE additions such as Gd^{3+}, La^{3+}, and Y^{3+}. They concluded that the lowest ionic conductivities are obtained for Sc-containing materials. This effect was explained as a consequence of the higher dopant-vacancy binding energies for Sc-containing materials as compared to those of other trivalent substituents in the low and intermediate temperature regime. As a matter of fact, in this regime, thermodynamic effects strongly limit the equilibrium number of free and associated defects. In this regard, Kilner et al.[13] showed that this dopant-vacancy association can persist up to the high temperature regime, in which vacancies are expected to be "free" in the case of Sc-containing materials.

However, research in the area of Sc-doped ceria is quite scarce. This is mainly due to the low solubility limit of Sc in the Ce-lattice which has impeded the synthesis of a wide range of substituent concentrations. The main reason for this is the large difference in ionic radii of Sc^{3+} (0.87 Å) and Ce^{4+} (0.97 Å).[17] Furthermore, the low solubility of Sc_2O_3 has also been related to the strong association energy to vacancies, which can encourage clustering of Sc^{3+} and vacancies leading to phase segregation.[18]

Grover et al.[19] studied a series of $CeO_2-Sc_2O_3$ samples prepared by solid state reaction with the following compositions: $Ce_{1-x}Sc_xO_{2-x/2}$ with x ranging from 0 to 1. They reported a very small amount of Sc^{3+} incorporated to the CeO_2 lattice due to a slight decrease in the lattice parameter with respect to pure ceria. In fact, all Ce−Sc compositions synthesized exhibited phase segregation. On the other hand, Moure et al.[20] prepared 8 at. % Sc and 18 at. % Sc doped CeO_2 by chemical, mechanochemical, and solid state reaction routes. In this work, the fresh samples exhibited phase segregation, which was considerably reduced with several hours of powder milling. However, small traces of Sc_2O_3 could still be detected in XRD patterns. Finally, Lee et al.[21] synthesized a series of $CeO_2-Sc_2O_3$ samples with nominal compositions of $Ce_{1-x}Sc_xO_{2-\delta}$ with x = 0.01, 0.03, 0.07, 0.1, and 0.2 by a polymerized complex method. They reported phase segregation for 20 at. % Sc composition. Nonetheless, lattice parameters obtained for the remaining compositions did not exhibit a linear decay with dopant concentration, indicating there might be some Sc-rich secondary phase. In all reported cases, lattice parameters are significantly higher than the theoretical ones for a $Sc_2O_3-CeO_2$ solid solution, in contrast with those corresponding to other RE-ceria doped solid solutions.[22]

Co-substitution became an intensely investigated strategy in the past few years to increase ionic conductivity in ceria-doped materials.[22] In early reports, the main objective has been to reproduce the ideal ionic radius proposed by Kim et al.[5] that would minimize lattice strains due to contraction/expansion, what is expected to enhance ion conductivity. In more recent publications the strategy has shifted to finding the ionic radius that minimizes oxygen vacancy ordering, one of the mechanisms responsible for the drop in conductivity in ionic conductors.[23,24] However, recent evidence disprove the existence of synergistic effects in ionic radius optimization for increasing ionic conductivity. In fact, an average conductivity of the single-doped materials is obtained.[22]

In this work we intend to pursuit another codoping strategy which is to combine the enhanced thermal stability provided by the ZrO_2 with an increase in vacancy concentration through Sc addition. We aim to analyze the effects of the combined additions of Sc_2O_3 and ZrO_2 in the Ce-rich region of the phase diagram on structural, morphological, and, especially, redox properties of the substituted lattice. We expect that vacancy generation through aliovalent substitution will improve the oxygen release capacity of the material. Therefore, in situ X-ray absorption experiments were performed using a synchrotron source to assess the reducibility of the samples in reducing atmospheres. It is worth mentioning that no previous reports on this ternary system were published in the literature. A soft chemical route that enabled nanometric-sized powder synthesis, such as the citrate complexation method, was selected to increase Sc solubility in the Ce lattice.

2. EXPERIMENTAL SECTION

2.1. Sample Preparation. Synthesis of Ce−Zr−Sc Nanopowders. The $Ce_{0.9}Sc_xZr_{0.1-x}O_{2-\delta}$ (x = 0, 0.02, 0.04, 0.06, 0.08, and 0.1) mixed oxides were synthesized from nitrate precursors by complexing the metal cations with citrate ions. Cerium nitate (Alfa Aesar, 99.5%), zirconyl nitrate (Sigma-Aldrich, 99%), and scandium nitrate (Standford Materials, 99.99%) were employed as precursors.

Nitrates were dissolved in distilled water and stirred for 4 h. Afterward, citric acid ($C_6H_8O_7{\cdot}H_2O$, Merck, 99.5%) was added to the solution with a molar ratio of metal cations to citric acid of 1:1 in all cases. The mixture was then stirred for 2.5 h in order to dissolve all precursors at room temperature. Evaporation of water took place for 17 h at 90 °C. First a transparent gel was obtained and then, after removing excess water, a yellowish powder was formed. Temperature was then increased up to 140 °C, at which point the decomposition of the precursors took place and nitrogen oxides were removed, giving rise to a powder mixed with carbonaceous residues. Finally, the remnant powder and ashes were calcined at 500 °C in static air for 2 h following a 10 °C/min heating rate.

2.2. Scanning Electron Microscopy. Scanning electron microscopy (SEM) experiments were carried out to assess the morphology of the synthesized samples. SEM images were obtained with a Zeiss Electron Beam SEM-Supra 40. The powdered samples were placed over an adhesive carbon-filled conductive tape to avoid charging problems.

2.3. Isothermal Nitrogen Physisorption. Textural characterization associated with porosity was performed by means of nitrogen adsorption−desorption isotherms obtained at 77 K. The experiments were carried out in a Quantachrome Corporation Autosorb-1 equipment. Samples were previously degassed with He at 50 °C for 12 h under vacuum conditions. Specific surface area was calculated by means of the five point Brunauer−Emmett−Teller (BET) method with the adsorption

DOI: 10.1021/acs.jpcc.6b07847
J. Phys. Chem. C 2016, 120, 24165−24175

points of the isotherm in the following relative pressure range: 0.05−0.35.

Average particle size was estimated using the following expression $D_{BET} = 6\rho^{-1}S_{BET}^{-1}$, where ρ is the theoretical density of the sample obtained from X-ray powder diffraction (XPD) patterns after Rietveld refinements and S_{BET} is the specific surface area. Particles are assumed to be spherical for this calculation.

2.4. Small-Angle X-ray Scattering. The porous structure was also analyzed by means of the small-angle X-ray scattering (SAXS) technique with a Bruker NanoStar equipment with a 2D Vantec Hi-Star detector coupled with a Cu Kα (λ = 0.154 18 nm) X-ray source. This camera has a microfocus Genix 3D system (source + focusing mirrors) and two scaterless slits sets for collimation. Operating conditions were of 50 kV and 0.6 mA with a sample-to-detector distance of 0.667 m. Exposure time to radiation was of 1800 s in a vacuum chamber.

Powder samples were tested in a cell enclosed between two thin mica windows. SAXS intensity curves were determined as a function of the modulus of the scattering vector [$q = (4\pi/\lambda) \sin \theta$], being θ half the scattering angle and λ the X-ray wavelength used in the experiments. Parasitic scattering due to air and slit was subtracted, and a spatial correction was performed due to the 2D detector plate. The resultant scattering curves were corrected to account for sample absorption. No mathematical desmearing processing was applied to SAXS curves due to small beam cross section and pixel size.

The software GNOM[25,26] was used to analyze the experimental curves. The volume-weighed pore radius distribution was determined by assuming a two-electron density model composed of a homogeneous matrix in which a diluted set of polydisperse spheres are embedded.

2.5. X-ray Powder Diffraction. The crystallographic structure was studied by means of X-ray powder diffraction (XPD), using a Bruker Discover DaVinci D8 diffractometer operated with Cu Kα radiation at 40 kV and 30 mA and a Ni filter in Bragg−Brentano configuration. Experimental data were collected in the angular 2θ range of 20°−100° with a step size of 0.02° and a time per step of 5 s. Rietveld refinements were conducted by using the Fullprof Suite Software.[27] In all refinements the fluorite structure was fitted: $Fm\bar{3}m$ space group, with Ce^{4+}, Zr^{4+}, and Sc^{3+} cations in 4a positions and O^{2-} anions in 8c positions. The occupation factors of Ce, Zr, and Sc were set, at the beginning of the refinement, to be equal to the nominal amounts of the cations in each sample. In all cases, after refinement the occupation factors remained invariant, thus indicating that these values were adequately a priori selected Oxygen stoichiometry was fixed during the refinements to the theoretical amount of oxygen in the lattice that corresponds to the amount of aliovalent cation (Sc^{3+}) incorporated into the CeO_2−ZrO_2 lattice in each sample.

The peak shape was simulated using a pseudo-Voigt function, and the background of each profile was fitted using a six-coefficient polynomial function. Isotropic atomic temperature parameters were used. The results of these refinements led to the determination of lattice parameters and associated densities.

The average crystallite size was estimated using the Scherrer equation: $D_{XPD} = 0.9\ \lambda/\beta \cos(\theta)$, where D_{XPD} is the crystallite size, λ is de Cu Kα radiation wavelength (0.154 18 nm), θ is the Bragg peak angular position, and β is the corrected peak width at half-maximum intensity. Peak width was corrected using the following formula: $\beta = \beta_s - \beta_i$, where β_s is the measured width for the (111) peak of each sample and β_i is the instrumental broadening determined with a Si standard.

2.6. Temperature-Programmed Reduction (TPR) Experiments. TPR experiments were performed in a Micromeritics Chemisorb 2720 equipment in order to study the reducibility of the samples. TPR runs went from ambient temperature up to 800 °C with a heating ramp of 10 °C min^{-1} in a flow of 5 mol % H_2 in Ar (50 cm^3 (STP) min^{-1}). Samples were pretreated before each measurement in order to eliminate any species that might have been adsorbed on the solid surface. Degassing was performed for 1 h in pure He flow at 300 °C with heating and cooling rates of 10 °C min^{-1}. The equipment determines the H_2 uptake with a thermal conductivity detector (TCD) previously calibrated.

However, the amount of reducible species in the samples does not exceed 37 wt % due to the reduction reaction stoichiometry, and therefore the signal-to-noise ratio in the yielded intensity was not good enough to quantify the degree of reduction with the generally recommended amounts of sample.[28] As a consequence, to enhance signal-to-noise ratio in TPR profiles, a sample mass of 80 mg was used in each test and the profiles were analyzed for comparative purposes. Therefore, in order to obtain the degree of reduction of the samples quantitatively, in situ XANES experiments described in the next section were performed.

2.7. In Situ XANES/TPR Experiments. In situ X-ray absorption near-edge structure (XANES) spectra associated with TPR characterization were measured in the Ce L_{III}-edge at the D06A-DXAS dispersive beamline of the National Synchrotron Light Laboratory (LNLS), Campinas, Brazil (Proposal: XAFS1-15329). A Si (111) monochromator was used altogether with a CCD detector to collect the absorption spectra in transmission mode. Self-supporting discs were prepared by mixing the sample powder with boron nitride, which has no significant absorption in the measured energy ranges. The sample mass in the discs was calculated in order to obtain a total absorption ratio of 1.5. In the experiments 12 mg of powdered sample and 73 mg of boron nitride were used.

The discs to be studied were located in a sample holder, with a thermocouple attached to it, inside a furnace with temperature control. The sample holder was placed in a quartz reactor with inlet and outlet gas lines. Inlet gas composition was set with a gas-mixing station provided with mass flow controllers and exit composition was assessed with a Pfeiffer Omnistar mass spectrometer. In situ TPR experiments were carried out by heating the sample in a 5 mol % H_2 (He balance) flow with a heating rate of 10 °C.min^{-1} up to 800 °C in order to emulate conventional laboratory TPR test conditions.

Data analysis was performed by means of the software Athena included in the IFEFFIT software package (Version 1.2.11).[29] A linear combination fitting of standard spectra was carried out in order to assess the fractions of reduced and oxidized species in the samples during the course of the experiments. Before proceeding with the linear combination fitting, background subtraction and spectrum normalization was carried out. The fittings were performed using a linear combination of the spectrum of $Ce(NO_3)_3$, as a Ce(III) standard, and the initial spectrum of each sample. It is important to mention that by following this procedure we obtain the degree of reduction achieved and not the absolute Ce(III) content.

DOI: 10.1021/acs.jpcc.6b07847
J. Phys. Chem. C 2016, 120, 24165−24175

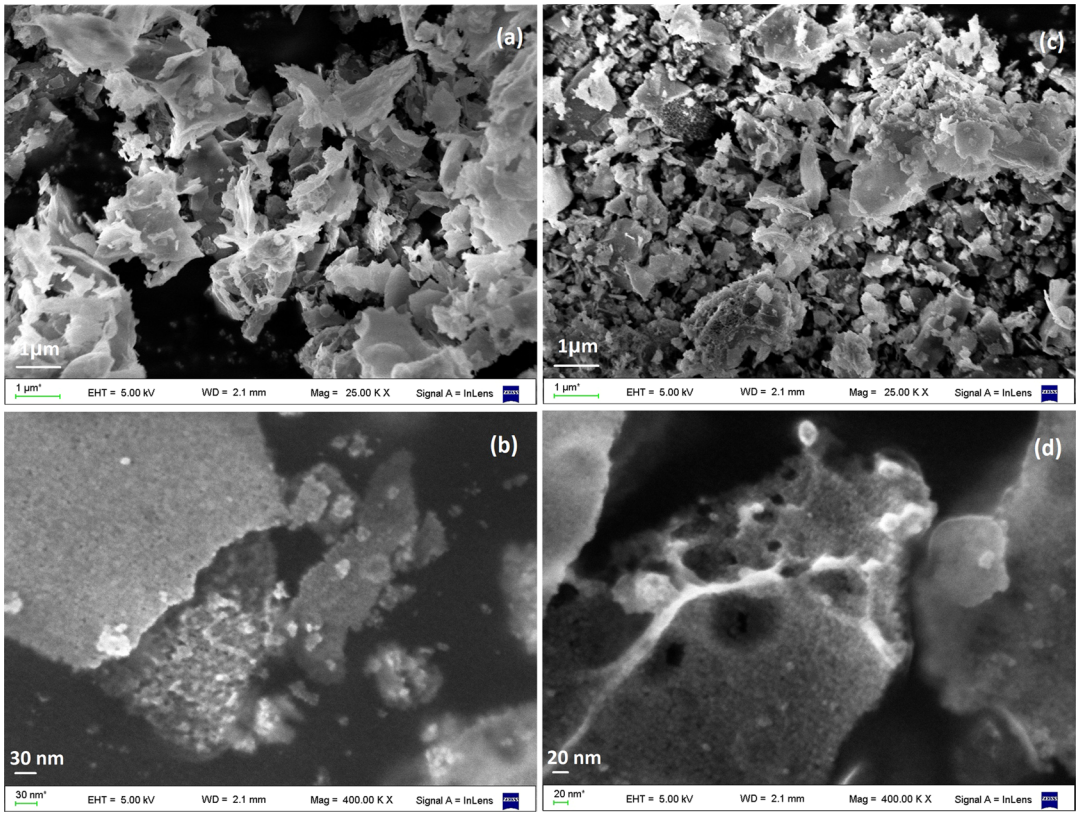

Figure 1. SEM micrographs for samples: (a, b) $Ce_{0.9}Zr_{0.1}O_2$ and (c, d) $Ce_{0.9}Zr_{0.04}Sc_{0.06}O_{1.97}$ fired at 500 °C.

3. EXPERIMENTAL RESULTS

3.1. Powder Morphology. SEM images with different magnifications of $Ce_{0.9}Zr_{0.1}O_2$ and $Ce_{0.9}Zr_{0.04}Sc_{0.06}O_{1.97}$ samples are shown in Figure 1. In Figures 1a and 1c the overall morphology can be observed which consists mainly of large thin flakes. In Figures 1b and 1d, with a higher magnification, small grains in the nanometric domain are observed as parts of the walls of platy particles.

All samples exhibited similar morphology with no significant differences. This shows that the employed synthesis method is reproducible and that the partial and total substitution of 10 at. % Zr with Sc does not produce significant changes in sample morphology.

3.2. Porosity Characterization Studied by N_2 Physisorption. The results of textural characterization including nitrogen adsorption and desorption isotherm branches are plotted in Figure 2. For clarity a limited number of isotherms are depicted, the others being very similar to those exhibited in Figure 2. The curves plotted in Figure 2 display a type H3 hysteresis loop according to IUPAC classification.[30] This hysteresis loop is characteristic of aggregates of platelike particles with delayed capillary condensation. The main feature in this loop is that it does not close until the equilibrium pressure is near or at the saturation pressure. In addition to this, the isotherms obtained also present a very narrow range of relative pressure before the characteristic linear zone of the adsorption branch, indicating low adsorption in the micropore range.

Results from the analysis of the isotherms are presented in Table 1. BET specific surface values are highest for samples $Ce_{0.9}Zr_{0.06}Sc_{0.04}O_{1.98}$ and $Ce_{0.9}Sc_{0.1}O_{1.95}$ (56 and 57 $m^2\ g^{-1}$, respectively) and lowest for sample $Ce_{0.9}Zr_{0.08}Sc_{0.02}O_{1.99}$ (38

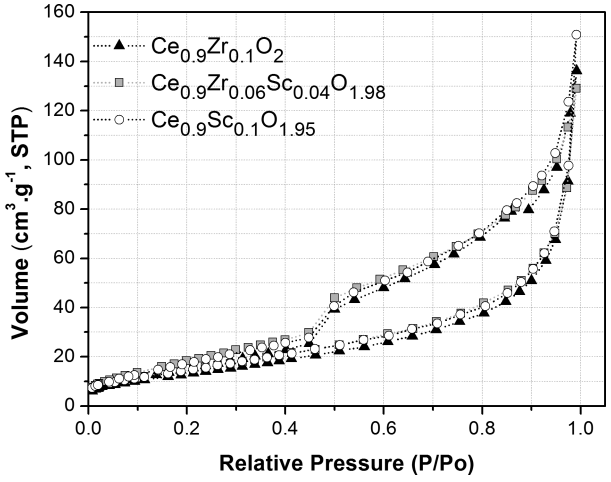

Figure 2. N_2 adsorption−desorption isotherms at 77 K for samples $Ce_{0.9}Zr_{0.1}O_2$, $Ce_{0.9}Zr_{0.06}Sc_{0.04}O_{1.98}$, and $Ce_{0.9}Sc_{0.1}O_{1.95}$.

Table 1. Textural Characterization Results from N_2-Physisorption Isotherms

sample	BET surface area (m^2/g)	total pore vol (cm^3/g)	av pore width BJH (nm)
$Ce_{0.9}Zr_{0.1}O_2$	51	0.211	16.6
$Ce_{0.9}Zr_{0.08}Sc_{0.02}O_{1.99}$	38	0.201	21.4
$Ce_{0.9}Zr_{0.06}Sc_{0.04}O_{1.98}$	56	0.200	14.3
$Ce_{0.9}Zr_{0.04}Sc_{0.06}O_{1.97}$	42	0.189	18.1
$Ce_{0.9}Zr_{0.02}Sc_{0.08}O_{1.96}$	44	0.212	19.2
$Ce_{0.9}Sc_{0.1}O_{1.95}$	57	0.234	16.3

DOI: 10.1021/acs.jpcc.6b07847
J. Phys. Chem. C 2016, 120, 24165−24175

$m^2.g^{-1}$). Adding Sc to the Ce−Zr system slightly diminishes total pore volume for samples with Sc contents up to 6 at. % and then increases for samples with higher Sc concentrations ($Ce_{0.9}Zr_{0.02}Sc_{0.08}O_{1.96}$ and $Ce_{0.9}Sc_{0.1}O_{1.95}$). The t-plot method results (not presented in the table) showed a negative *y*-intercept in the volume vs t-plot curve. This altogether with the isotherm shape, low *C* values obtained in BET analysis ($23 < C < 41$), and external surface area similar to BET area indicates no significant contribution of micropores to total pore volume.[31]

Pore size distributions calculated by means of the BJH model with the desorption branch of the isotherms are presented in Figure 3. All samples present broad size distributions in the

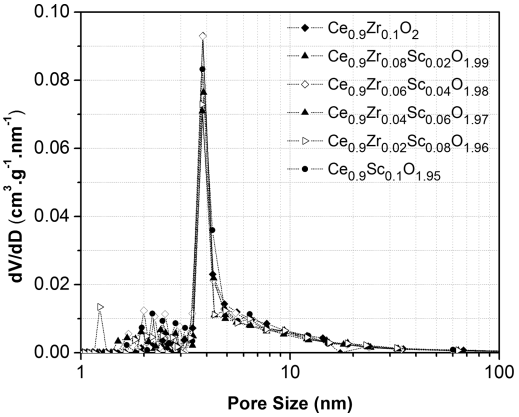

Figure 3. Pore size distribution of all samples calculated applying BJH model to the desorption branch of N_2-physisorption isotherms.

mesopore region (2−50 nm) with a maximum at ca. 4 nm. Average pore widths presented in Table 1 are well correlated with specific surface areas, being narrower for samples with higher BET areas such as $Ce_{0.9}Zr_{0.06}Sc_{0.04}O_{1.98}$ and $Ce_{0.9}Sc_{0.1}O_{1.95}$ with an average pore width of 14.3 and 16.3 nm, respectively.

Figure 4 exhibits the pore size distributions calculated with the BJH model for both adsorption and desorption branches of the isotherm obtained for sample $Ce_{0.9}Zr_{0.04}Sc_{0.06}O_{1.97}$. Analogous results were obtained with the other compositions.

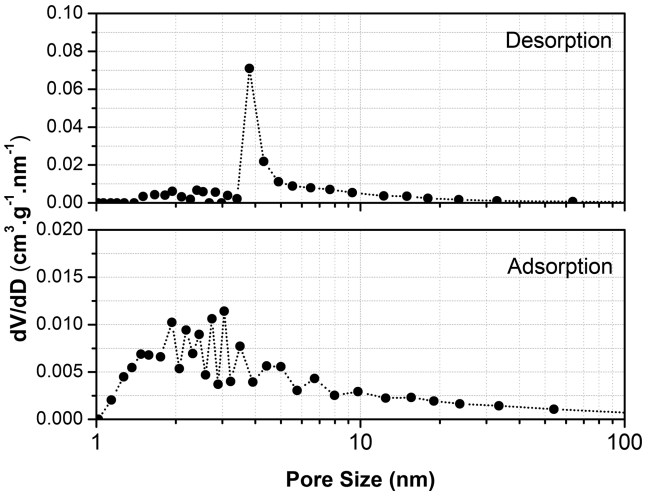

Figure 4. Pore size distribution calculated applying BJH model to adsorption and desorption branches of N_2-physisorption isotherm of the $Ce_{0.9}Zr_{0.04}Sc_{0.06}O_{1.97}$ sample.

Results are slightly different for the adsorption branch if compared to the desorption one, since the distribution is broader and starts at pores with lower average width.

The fact that adsorption and desorption branches presented actual pore size distributions implies that the peak maximum obtained with the BJH model is not a result of the tensile strength effect but rather a proof of real pore size distribution.[32] However, the visible differences can be attributed to the delayed capillary condensation, characteristic of type H3 hysteresis loops. In fact, as the isotherm does not exhibit a plateau at high P/P_0 values, mesopore volume cannot be reliably assessed by the BJH method. Therefore, to gain further insight into pore volume distribution, additional experiments were carried out by means of SAXS technique, and the results are presented in the next section.

3.3. Porosity Characterization Studied by SAXS. In order to gain further insight into pore size distribution, SAXS measurements were performed. Experimental SAXS intensity curves as functions of the modulus of the scattering vector, $I(q)$, corresponding to all studied samples are plotted in Figure 5.

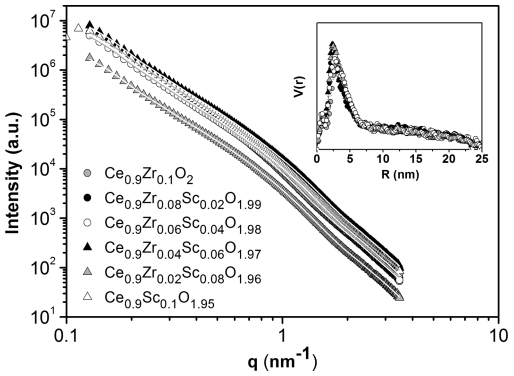

Figure 5. Small-angle X-ray scattering (SAXS) experimental curves (symbols) in log−log scale and GNOM fitting results (solid lines). Inset: volume-weighted pore size distribution derived from GNOM analysis.

The experimental SAXS curves were analyzed by using GNOM software[25,26] assuming that the system can be well described as a dilute and polydisperse set of spherical pores. Figure 5 exhibits together the experimental SAXS curves (symbols) and the modeled curves (solid lines) derived from GNOM output. The volume weighted pore radius distributions V(R), also derived from GNOM, are shown in an inset.

We can notice in Figure 5 that the modeled SAXS curves are in good agreement with the experimental SAXS curves, thus suggesting that the proposed pore model describes suitably the relevant features of pore structure.

The volume distribution functions, $V(R)$, derived from GNOM and displayed in the inset of Figure 5 indicate for all samples the presence of a main pore mode centered at circa R = 3.0 nm and a very wide distribution of larger pores. The main mode has been assigned to the presence of small pores located inside the powder particles and the wide distribution of larger pores to those located between particles. The main mode of small pores and the wide distribution of larger pores are named as intraparticle pores and interparticle pores, respectively. As it will be shown in the next section, the particles of the powder samples are composed of crystallites with an average size of 5.0 nm circa. Thus, the main pore mode centered at 3.0 nm

DOI: 10.1021/acs.jpcc.6b07847
J. Phys. Chem. C 2016, 120, 24165−24175

Table 2. Lattice Parameter and Rietveld Refinement Results, Average Crystallite Size (D_{XPD}), Particle Size (D_{BET}), and Degree of Agglomeration (D) for All Synthesized Samples

sample	lattice parameter (Å)	χ^2	R_p	R_{wp}	R_{exp}	ρ_{THEO} (kg/m^3)	D_{BET} [a] (nm)	D_{XRD} [b] (nm)	$D = D_{BET}/D_{XRD}$
$Ce_{0.9}Zr_{0.1}O_2$	5.388(2)	1.27	4.66	5.27	4.67	7103	16.6	7.0	2.4
$Ce_{0.9}Zr_{0.08}Sc_{0.02}O_{1.99}$	5.385(4)	1.53	3.73	4.21	3.40	7068	15.4	6.1	2.5
$Ce_{0.9}Zr_{0.06}Sc_{0.04}O_{1.98}$	5.384(8)	1.37	3.93	4.07	3.48	7024	15.2	6.1	2.5
$Ce_{0.9}Zr_{0.04}Sc_{0.06}O_{1.97}$	5.383(5)	1.46	3.68	4.17	3.45	6983	20.5	5.9	3.5
$Ce_{0.9}Zr_{0.02}Sc_{0.08}O_{1.96}$	5.381(8)	1.26	4.95	5.64	5.03	6943	19.5	5.8	3.4
$Ce_{0.9}Sc_{0.1}O_{1.95}$	5.385(2)	1.47	3.75	4.27	3.52	6884	15.2	5.8	2.6

[a]Calculated from specific surface area. [b]Calculated using Scherrer equation with peak (111).

(intraparticle pores) is reasonably expected for agglomerated 5 nm sized crystals.

The conclusion related to the presences of a main mode associated with intraparticle pores at circa R = 3.0 nm and a wide distribution of larger interparticle pores derived from SAXS results is consistent with the results corresponding to N_2-physisorption isotherms displayed in Figure 3, in which a narrow mode of small pores and a wide distribution of larger pores are apparent. This result is also consistent with those reported in Table 2 in which the degrees of agglomeration (D) are in all cases higher than 1.

Thus, the results derived from SAXS and N_2-physisorption isotherms together with those derived from XRD measurements indicate, all of them, that small nanometric crystallites agglomerate and form particle aggregates of larger sizes.

3.4. Crystallographic Characterization. XRD profiles corresponding to all studied samples are plotted in Figure 6.

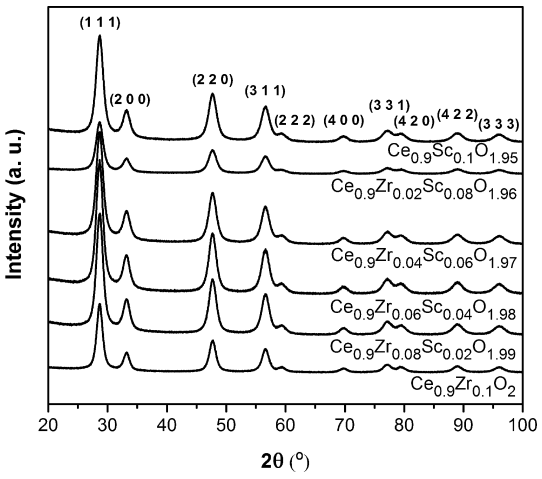

Figure 6. XRD patterns of samples synthesized by citrate route after firing at 500 °C.

Peak assignments revealed that all samples exhibit a cubic fluorite-type structure, i.e., the same as that of cerium dioxide. The observed very broad Bragg peaks indicate that the studied powders are composed of small crystallites with sizes within the nanometric range. Furthermore, the peaks are symmetric, suggesting that the samples are homogeneous in composition. No other Bragg peaks were detected, this finding suggesting the absence of any other minor crystalline species.

The average crystallite sizes of all samples are reported in Table 2. We can notice a slight difference in this value when sample $Ce_{0.9}Zr_{0.1}O_2$ is partially or totally substituted with Sc, whereas no significant difference is observed for samples with different Sc content. The degree of agglomeration ($D = D_{BET}/D_{XRD}$) reported in Table 2, in all cases, exceeds unity. These results are in qualitative agreement with SEM images, which show that small crystallites are agglomerated in the walls of flake-like particles.

Rietveld refinement results are summarized in Table 2 and in Figure 7. In Figure 7 the lattice parameter is plotted against

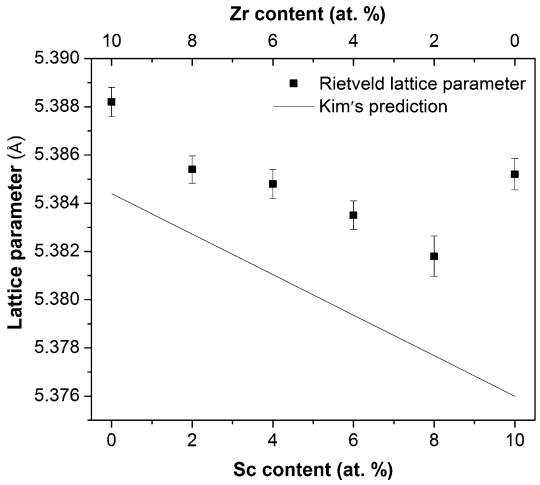

Figure 7. Lattice parameters of $Ce_{0.9}Zr_{(0.1-x)}Sc_xO_{2-\delta}$ determined by Rietveld refinements as a function of Sc and Zr atomic contents (symbols) and expected values derived from Kim theory (solid line).[5]

scandium atomic content, which exhibits a linear decrease with additive content up to 8 at. % Sc and a higher than expected increase for $Ce_{0.9}Sc_{0.1}O_{1.95}$ sample. Kim et al.[5] proposed an empirical equation that estimates the lattice parameter for substituted ceria powders as a function of dopant concentration. This prediction is plotted in Figure 7 altogether with the experimental results. The slope of the linear trend of lattice parameter versus substituted atom concentration predicted by Kim is in very good agreement with the slope of the refined values for all samples except for $Ce_{0.9}Sc_{0.1}O_{1.95}$ sample. This suggests that up to 8 at. % Sc the cations are fully incorporated into de Ce lattice. The reason why the predicted values are lower than the measured ones might be related to the fact that Kim obtained the empirical correlation for micrometer-sized powders, while the samples here presented are nanometric.

On the other hand, the fact that the linear trend in the lattice parameter vs substituted cation concentration plot is disrupted for $Ce_{0.9}Sc_{0.1}O_{1.95}$ sample could imply that Sc was not fully incorporated into the lattice. Although XRD patterns show no evidence of phase segregation, small clusters of Sc_2O_3 with limited long-range ordering might have been formed resulting in no reflections for the secondary phase.

DOI: 10.1021/acs.jpcc.6b07847
J. Phys. Chem. C 2016, 120, 24165−24175

In order to estimate the amount of Sc that was effectively incorporated into the lattice in sample $Ce_{0.9}Sc_{0.1}O_{1.95}$, a calculation was performed by means of Kim's empirical formulation. To do so, the theoretical *y*-intercept in the lattice parameter vs Sc content plot from Kim's formulation was transformed to the experimental value obtained for $Ce_{0.9}Zr_{0.1}O_2$ sample (0 at. % Sc), while maintaining the predicted slope. This correction was performed in order to account for the difference in the lattice parameter of pure microcrystalline ceria considered by Kim compared to the value of nanosized ceria. Once this correction was completed, the effective amount of Sc incorporated which could yield the experimental lattice parameter obtained was estimated to be 8.5 ± 0.2 at. %. Therefore, in the case of $Ce_{0.9}Sc_{0.1}O_{1.95}$, an additional amount of Sc was incorporated when compared to sample $Ce_{0.9}Zr_{0.02}Sc_{0.08}O_{1.96}$, leading to a slight expansion in the lattice parameter due to the absence of Zr in the lattice.

It is interesting to notice that available literature for CeO_2–Sc_2O_3 system acknowledges a very low solubility limit for Sc^{3+} in the CeO_2 lattice. Gerhardt et al.[11] reported a maximum 3 at. % Sc solubility for samples prepared by a coprecipitation method with a sintering temperature of 1500 °C. On the other hand, Grover et al.[19] studied $Ce_{1-x}Sc_xO_{2-x/2}$ samples with $x > 0.1$ by solid state reaction and further sintering at $T > 1200$ °C, and even for the lowest Sc-containing sample, traces of Sc_2O_3 could still be detected by XRD. Moure et al.[20] studied 8 and 18 at. % Sc doped ceria synthesized by several methods, and in all cases, the as-synthesized samples exhibited Sc_2O_3 segregation. In their work, Sc incorporation to the lattice was enhanced by means of milling the powders for several hours which reduced the crystallite size from 91 to 13 nm.

Burbano et al.[22] studied the effect of ceria codoping with several rare earth elements by means of computer simulations and compared predicted lattice parameters with experimental results reported in the literature. These authors calculated the lattice parameter as a function of ionic radius. All RE-ceria experimental points taken from literature data matched very well their predictions, except for the Sc-substituted ceria ($Ce_{0.9}Sc_{0.1}O_{1.95}$) values.[22] All experimental values reported for this sample were well above the theoretical lattice parameter of ca. 5.378 Å, while in our work, the measured lattice parameter for the same sample composition was of 5.385(2) Å, which is quite close to that value and, by far, the closest reported in the literature. Grover et al.[19] reported a lattice parameter a = 5.403(1) Å while Moure et al.[20] a = 5.41(3) Å, both very close to that of pure microcrystalline ceria.

We emphasize that the samples studied in our investigation were prepared by the citrate complexation synthesis route and calcined at mild temperatures (T_c = 500 °C). This enabled us to obtain powders with crystallite sizes as small as 6 nm circa with no evidence of phase segregation and with a wider range of Sc solubility in the ceria lattice (up to 8 at. % Sc).

3.5. Temperature-Programmed Reduction. Ex Situ Experiments. TPR profiles of all samples are shown in Figure 8. Two main features can be clearly distinguished in the $Ce_{0.9}Zr_{0.1}O_2$ TPR profile, namely, two reduction peaks at 546 and 733 °C. In the past, CeO_2 and Ce–Zr reduction profiles have been widely studied in conventional laboratory TPR experiments, and there is general consensus regarding the main observed features in the reduction profile, which are usually ascribed to the reduction of surface and bulk species.[33,34]

In CeO_2 reduction, the initial step is attributed to the reduction of surface species and is closely related, first, to the kinetics and thermodynamics of the reduction reaction and, second, to morphological changes in the samples due to sintering effects, which are triggered by the increasing temperature and reducing atmospheres.[35] In the second step, in which reduction in the bulk takes place, oxygen diffusion phenomena play a relevant role in defining the profiles that are obtained.

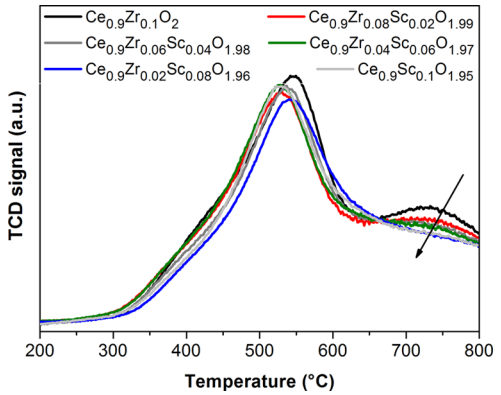

Figure 8. Temperature-programmed reduction (TPR) profiles measured as the signal of a thermal conductivity detector (TCD). The classical laboratory TPR experiments were carried out in 5 mol % H_2/Ar.

In this regard, in Figure 8, although the TCD signal corresponding to $Ce_{0.9}Zr_{0.1}O_2$ sample exhibits two well-defined peaks, which are attributed to surface and bulk reduction, the second peak becomes less apparent for other compositions. In fact, the intensity of the second peak diminishes with increasing Sc compositions, thus establishing a clear tendency for the whole set of samples. This occurs alongside with the shift in the peak position ascribed to surface reduction toward lower temperatures.

It is interesting to notice that all samples exhibit similar morphology and surface areas, which implies that the differences in the redox behavior cannot be attributed to changes in these features but most certainly to the capacity of exchanging oxygen from the lattice in a reducing atmosphere. Therefore, in order to quantitatively assess the reduction extent corresponding to each sample, further studies by means of in situ XANES/TPR experiments were performed, and their results will be reported in the next section.

3.6. In Situ XANES Measurements. In situ XANES spectra were collected during TPR experiments at the Ce LIII-edge. All samples were heated at 10 °C min^{-1} in a reducing feed flow of 5 mol % H_2/He as detailed in the Experimental Section. The reference spectra used to quantify the relative amount of Ce^{4+} and Ce^{3+} species during linear combination fitting are presented in Figure 9. In the case of Ce^{4+}, the initial spectrum under ambient air for each sample was taken as a reference. In Figure 9 two well-defined absorption peaks located close to the absorption edge are apparent, which were attributed to characteristic electronic transitions of Ce^{4+} compounds, namely $2p_{3/2} \rightarrow (4f^1L)5d^*$ and $p_{3/2} \rightarrow (4f^0)5d^*$ transitions.[35]

In the case of Ce^{3+}, a $Ce(NO_3)_3$ sample was used to obtain a reference spectrum of the reduced species. In this spectrum, only one absorption peak near the absorption edge is apparent, which was assigned to the $2p_{3/2} \rightarrow (4f^1)5d^*$ electronic transition corresponding to Ce^{3+} compounds.

Several XANES spectra recorded for some of the studied samples at selected temperatures during the TPR experiments

DOI: 10.1021/acs.jpcc.6b07847
J. Phys. Chem. C 2016, 120, 24165–24175

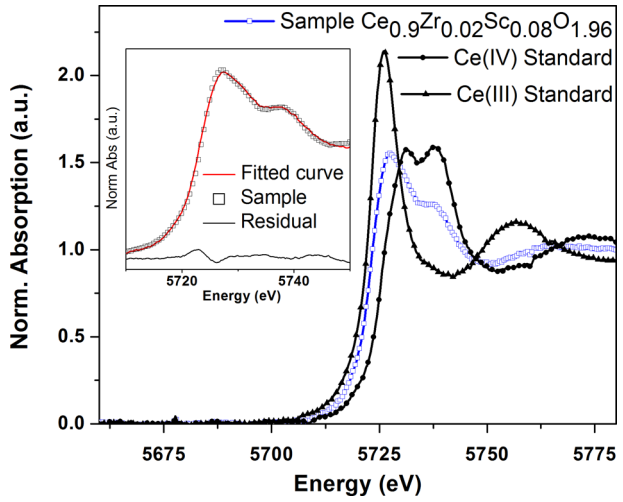

Figure 9. Ce(IV) and Ce(III) standards plotted altogether with a $Ce_{0.9}Zr_{0.02}Sc_{0.08}O_{1.96}$ spectrum recorded at 697 °C. In the inset the sample spectrum (squares) and the fitted curve (solid line) are plotted in the energy range in which the fittings were performed which correspond to the XANES region.

are depicted in Figure 10. At room temperature all samples are oxidized thus exhibiting the two characteristic absorption peaks with essentially the same maximum values, corresponding to CeO_2, while at the end of the experiments and maximum temperature (T = 800 °C) in reducing atmosphere, samples exhibit two absorption peaks with different relative maximum values, thus indicating the presence of both Ce^{3+} and Ce^{4+} species.

As an example, in Figure 9 both Ce(IV) and Ce(III) XANES standards are plotted as functions of photon energy altogether with an experimental spectrum recorded at 697 °C from sample $Ce_{0.9}Zr_{0.02}Sc_{0.08}O_{1.96}$. In the inset, the fitting result of the linear combination is displayed, which is in good agreement with experimental data within the relevant photon energy range (absorption edge ±20 eV). It should be mentioned that the maximum error in the Ce^{3+} and Ce^{4+} fractions calculated through fitting was in all cases of 0.5%.

Results derived from in situ XANES/TPR profiles are presented in Figure 11. The curves plotted in Figure 11 show the degree of Ce reduction in the samples (α) as a function of temperature. These values were calculated from XANES spectra by the fitting procedure previously detailed in the Experimental Section. In the first case, sample $Ce_{0.9}Zr_{0.1}O_2$ exhibited a reduction profile with two clear steps. The first increasing step ranges approximately from 0 to 30% reduction, and the second increasing step reaches a final degree of reduction of 52.6%. This two-step reduction profile is consistent with the results obtained from conventional laboratory TPR experiments reported in the previous section and can be ascribed, accordingly, to the successive reduction of surface and bulk ceria.

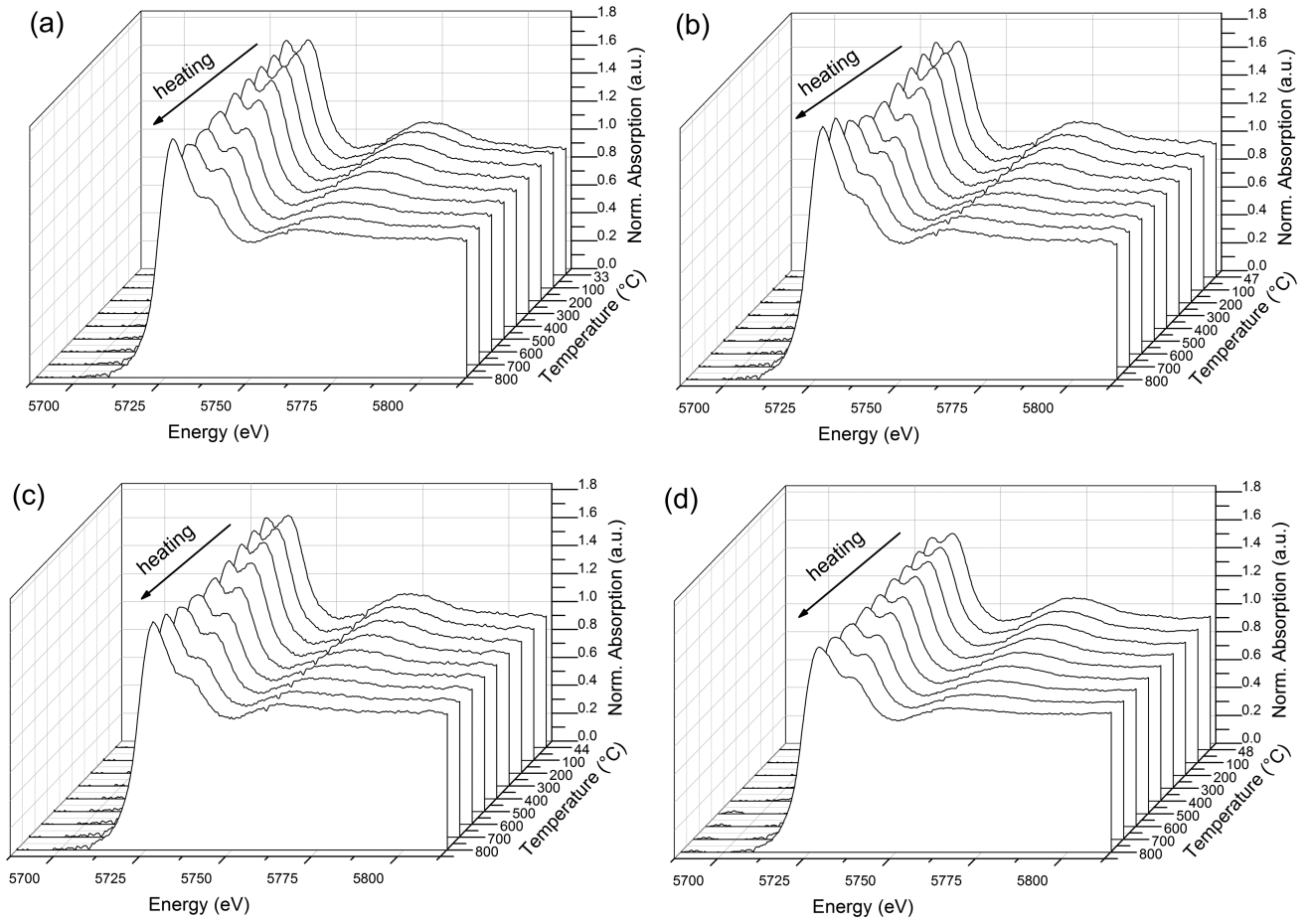

Figure 10. In situ XANES spectra for different temperatures, on heating, under a 5 mol % H_2/He atmosphere. Spectra corresponding to four selected samples are displayed: (a) $Ce_{0.9}Zr_{0.1}O_2$, (b) $Ce_{0.9}Zr_{0.06}Sc_{0.04}O_{1.98}$, (c) $Ce_{0.9}Zr_{0.04}Sc_{0.06}O_{1.97}$, and (d) $Ce_{0.9}Sc_{0.1}O_{1.95}$.

DOI: 10.1021/acs.jpcc.6b07847
J. Phys. Chem. C 2016, 120, 24165−24175

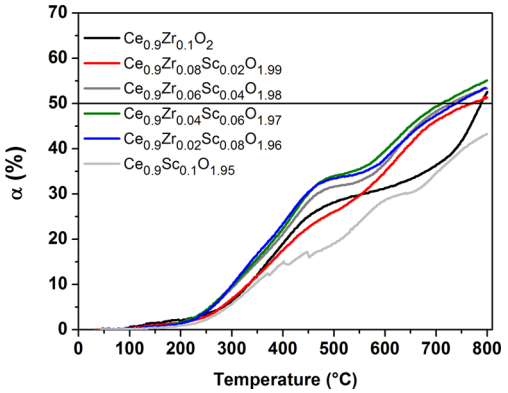

Figure 11. Degree of reduction, α (%), for increasing temperatures derived from in situ XANES/TPR experiments in 5 mol % H_2/He. The sample compositions are indicated.

4. DISCUSSION

The kinetics of the reduction process corresponding to all ternary compositions ($Ce_{0.9}Zr_{0.08}Sc_{0.02}O_{1.99}$, $Ce_{0.9}Zr_{0.06}Sc_{0.04}O_{1.98}$, $Ce_{0.9}Zr_{0.04}Sc_{0.06}O_{1.97}$, and $Ce_{0.9}Zr_{0.02}Sc_{0.08}O_{1.96}$) turned out to be clearly faster than that of $Ce_{0.9}Zr_{0.1}O_2$ over most of the temperature range, especially above 500 °C, where markedly higher reduction percentages were obtained. In particular, reduction profiles for samples $Ce_{0.9}Zr_{0.06}Sc_{0.04}O_{1.98}$, $Ce_{0.9}Zr_{0.04}Sc_{0.06}O_{1.97}$, and $Ce_{0.9}Zr_{0.02}Sc_{0.08}O_{1.96}$ were shifted to lower temperatures when compared to the $Ce_{0.9}Zr_{0.1}O_2$ profile, evidencing a noteworthy enhancement in the oxygen release capacity of Sc-containing samples. Finally, the reduction profile of $Ce_{0.9}Sc_{0.1}O_2$ exhibits what seems to be a three-step reduction profile with the lowest reduction values over all the temperature range.

A three-step reduction profile has been previously reported[33] in conventional laboratory TPR experiments. The first feature was ascribed to the reduction of surface species, while the second and third features were attributed to the reduction of bulk ceria. In fact, the third peak has been linked to the reduction of species existing in associated defects.[13] In the results presented here, the profiles of Sc-containing samples present a clear first reduction step followed by a less resolved second step, indicating that bulk reduction might include more than one reduction steps.

In fact, the second unresolved feature starts approximately when more than 40% of Ce^{3+} species are present in $Ce_{0.9}Zr_{0.06}Sc_{0.04}O_{1.98}$, $Ce_{0.9}Zr_{0.04}Sc_{0.06}O_{1.97}$, and $Ce_{0.9}Zr_{0.02}Sc_{0.08}O_{1.96}$ samples and to a lower reduction extent for $Ce_{0.9}Sc_{0.1}O_2$. The third feature in the TPR profile becomes more apparent for increasing Sc concentration, in agreement with the hypothesis arguing that defect association contributes to a third peak in the profile.

In the studied ternary system there are two competing mechanisms that might explain the different reduction profiles, namely (i) the influence of the formation of oxygen vacancies due to the presence of reduced ceria and (ii) oxygen vacancy formation due to the incorporation of trivalent cations (Sc^{3+}) to the $Ce_{0.9}Zr_{0.1}O_2$ lattice.

In the first case, defect−defect interactions in reducing environment are responsible for limiting oxygen diffusion in the ceria bulk lattice. In this context Yuan et al.[14] studied the effect of oxygen vacancy concentration in nonstoichiometric ceria upon reduction, by means of molecular dynamics simulations and reported a maximum in oxygen diffusivity vs vacancy concentration. The enhancement is explained by long-range vacancy−vacancy interactions along the ⟨100⟩ direction in the crystal lattice.

In the second case, in which an aliovalent dopant is incorporated, the dopant-defect interaction should be carefully analyzed. At low temperatures, Coulomb forces promote the association of Sc^{3+} and a vacancy to form incompletely compensated pairs $(ScV_O)^*$.[12] At temperatures high enough, these pairs dissociate giving rise to ionic conductivity in the "free vacancy regime". The effective activation energy for ionic conductivity (H_σ) has been defined as composed mainly by two terms: $H_\sigma = H_m + H_A$, where H_m is the activation energy for migration of a vacancy and H_A is the association enthalpy of the vacancy to the dopant in a pair.

Sc^{3+} attracted much interest as a dopant due to the high ionic conductivity developed when incorporated in the ZrO_2 lattice. Nonetheless, when incorporated into the CeO_2 lattice, very low ionic conductivities were reported.[11] This effect was attributed to the elastic energy involved in the association enthalpy, which is larger when the size mismatch between dopant and host is greater.[13]

As already mentioned, the ionic conductivity exhibits a maximum as a function of concentration of doped CeO_2. In the low concentration range, conductivity increases due to the fluctuating electrostatic field generated by the incompletely compensated $(ScV_O)^*$ pairs and the remaining Sc′ in the lattice which encourages the V_O^{**} to migrate through the field.

However, in the high concentration range, the reason for the decrease in ionic conductivity when trivalent dopants substitute Ce in the lattice is the presence of oxygen vacancy traps induced by two or more M^{3+} ions in the nearest or next-nearest sites.[12] These clusters affect the mobility of vacancies as a consequence of the increase in activation energy due to a higher vacancy-trap binding energy. In particular, Sc exhibits the highest binding energies in ceramics of trivalent rare-earth doped ceria, thus showing that full association can persist even at high temperatures (>600 °C). However, no studies of codoping CeO_2 with both Sc^{3+} and Zr^{4+} have been performed.

Oxygen vacancies are added to nonstoichiometric $Ce_{0.9}Zr_{0.1}O_2$ by partially reducing ceria. On the contrary, in the other studied samples vacancy generation is attributed to both effects: aliovalent doping and ceria reduction. Therefore, as Sc content increases the amount of defects increases as well. If we consider that for every two created Ce^{3+}, one oxygen vacancy is formed and we add up the vacancies associated with every two incorporated by trivalent dopants (Sc^{3+}), the oxygen nonstoichiometry can be estimated.

The different degrees of reduction derived from XANES results for all studied samples are reported in Table 3 altogether with the final degree of reduction at the end of the TPR experiments at 800 °C. These results indicate that a maximum in the final degree of reduction, α = 55.1%, occurs for 6 at. % Sc of dopant concentration. This indicates that further increasing Sc concentration would result in a decrease in the oxygen release capacity in reducing atmospheres.

On the other hand, the amount of defects increases for progressively higher oxygen nonstoichiometry, its value increasing up to 8 at % Sc content because, although the degree of reduction is lower than that of $Ce_{0.9}Zr_{0.04}Sc_{0.06}O_{1.97}$, the initial vacancies generated due to aliovalent doping is larger. Finally, in $Ce_{0.9}Sc_{0.1}O_{1.95}$ the amount of defects at the end of the TPR experiment is reduced because this sample exhibits a lower final degree of reduction.

DOI: 10.1021/acs.jpcc.6b07847
J. Phys. Chem. C 2016, 120, 24165−24175

Table 3. Final Degree of Reduction (α) and Estimated Oxygen Nonstoichiometry (δ) before and after TPR Experiments

sample	α (%, T = 800 °C)	oxygen NS (δ, T = 25 °C)[a]	oxygen NS (δ, T = 800 °C)[b]
$Ce_{0.9}Zr_{0.1}O_2$	52.6	0	0.237
$Ce_{0.9}Zr_{0.08}Sc_{0.02}O_{1.99}$	51.5	0.01	0.242
$Ce_{0.9}Zr_{0.06}Sc_{0.04}O_{1.98}$	53.2	0.02	0.259
$Ce_{0.9}Zr_{0.04}Sc_{0.06}O_{1.97}$	55.1	0.03	0.278
$Ce_{0.9}Zr_{0.02}Sc_{0.08}O_{1.96}$	53.5	0.04	0.281
$Ce_{0.9}Sc_{0.1}O_{1.95}$	43.3	0.05	0.245

[a]Estimated from nominal atomic composition at ambient air. [b]Estimated from nominal atomic composition and degree of reduction at the end of TPR experiments (T = 800 °C, 5 mol % H_2/He atmosphere).

Therefore, our results indicate that a higher initial oxygen nonstoichiometry enhances sample reducibility up to 6 at. % Sc doping; thus, further addition of defects is expected to enhance defect−defect and dopant−defect interactions, which could explain the delay in the overall reduction kinetics. However, in order to achieve a deeper insight into this matter, additional studies of the local environment of Sc^{3+} and Zr^{4+} are required.

5. CONCLUSIONS

We have successfully incorporated Sc into the CeO_2−ZrO_2 lattice up to 8% at. Sc without any significant phase segregation. This high solubility limit was reached in nanostructured samples prepared by means of a soft chemical synthesis route involving citrate complexation, which gave rise to porous powders with crystallite sizes in the nanometer range. The high solubility limit achieved exceeds by far those reported in the literature for samples prepared by using other synthesis procedures.

The main structural features of all studied homogeneous and nanostructured CeO_2−ZrO_2−Sc_2O_3 ternary materials were characterized as functions of their composition, namely the crystallographic aspects by XRD, the fine porosity by N_2-physisorption and SAXS, and the degree of reduction by in situ XANES/TPR.

Finally, we have demonstrated that adding Sc^{3+} to the CeO_2−ZrO_2 binary system leads to a ternary material with enhanced reducibility, which becomes significantly higher than that of both binary materials ($Ce_{0.9}Sc_{0.1}O_{1.95}$ and $Ce_{0.9}Zr_{0.1}O_2$). This enhancement occurs over the whole temperature range but is more pronounced over the temperature range from 550 up to 800 °C.

AUTHOR INFORMATION

Corresponding Author

*Tel +54 11 4709-8158; e-mail slarrondo@citedef.gob.ar or slarrondo@unsam.edu.ar (S.A.L.).

Notes

The authors declare no competing financial interest.

ACKNOWLEDGMENTS

The PhD. scholarship granted by CONICET to Lucía M. Toscani is gratefully acknowledged. This work was supported by the National Synchrotron Light Laboratory (LNLS) under proposal XAFS1-15329 and received financial support from MINCyT-CAPES BR/11/red/02 (Argentina-Brazil), PIDDEF 011/11 and ANPCyT-PICT 2013 No. 1587 and PICT 2011 No. 1948 (Argentina). A. F. Craievich and M. C. A. Fantini are researchers of CNPq, Brazil.

REFERENCES

(1) Sun, C.; Li, H.; Chen, L. Nanostructured Ceria-Based Materials: Synthesis, Properties, and Applications. *Energy Environ. Sci.* **2012**, *5*, 8475−8505.

(2) Chatzichristodoulou, Ch.; Blennow, P. T.; Søgaard, M.; Hendriksen, P. V.; Mogensen, M. B. Ceria and its Use in Solid Oxide Cells and Oxygen Membranes. In *Catalysis by Ceria and Related Materials*, 2nd ed.; Trovarelli, A., Fornasiero, P., Eds.; Imperial College Press: London, 2013.

(3) Jacobson, A. J. Materials for Solid Oxide Fuel Cells. *Chem. Mater.* **2010**, *22*, 660−674.

(4) Zhu, T.; Flytzani-Stephanopoulos, M. Catalytic Partial Oxidation of Methane to Synthesis Gas over Ni−CeO_2. *Appl. Catal., A* **2001**, *208*, 403−417.

(5) Kim, D. J. Lattice Parameters, Ionic Conductivities, and Solubility Limits in Fluorite-Structure MO_2 Oxide (M = Hf^{4+}, Zr^{4+}, Ce^{4+}, Th^{4+}, U^{4+}) Solid Solutions. *J. Am. Ceram. Soc.* **1989**, *72*, 1415−21.

(6) Bonk, A.; Remhof, A.; Maier, A. C.; Trottmann, M.; Schlupp, M. V. F.; Battaglia, C.; Vogt, U. F. Low-Temperature Reducibility of $M_xCe_{1-x}O_2$ (M = Zr, Hf) under Hydrogen Atmosphere. *J. Phys. Chem. C* **2016**, *120*, 118−125.

(7) Pengpanich, S.; Meeyoo, V.; Rirksomboon, T. Catalytic Oxidation of Methane Over CeO_2−ZrO_2 Mixed Oxide Solid Solution Catalysts Prepared Via Urea Hydrolysis. *Appl. Catal., A* **2002**, *234*, 221−233.

(8) Di Monte, R.; Kaspar, J. Nanostructured CeO_2-ZrO_2 Mixed Oxides. *J. Mater. Chem.* **2005**, *15*, 633−648.

(9) Larrondo, S. A.; Vidal, M. A.; Irigoyen, B.; Craievich, A. F.; Lamas, D. G.; Fábregas, I. O.; Lascalea, G. E.; Walsöe de Reca, N. E.; Amadeo, N. Preparation and Characterization of Ce/Zr Mixed Oxides and their Use as Catalysts for the Direct Oxidation of Dry CH_4. *Catal. Today* **2005**, *107*, 53−59.

(10) Zimicz, M. G.; Larrondo, S. A.; Prado, R. J.; Lamas, D. G. Time-resolved In Situ XANES Study of the Redox Properties of $Ce_{0.9}Zr_{0.1}O_2$ Mixed Oxides. *Int. J. Hydrogen Energy* **2012**, *37*, 14881−6.

(11) Gerhardt-Anderson, R.; Nowick, A. S. Ionic Conductivity of CeO_2 with Trivalent Dopants of Different Ionic Radii. *Solid State Ionics* **1981**, *5*, 547−550.

(12) Wang, D. Y.; Park, D. S.; Griffith, J.; Nowick, A. S. Oxygen-ion Conductivity and Defect Interactions in Ytria-doped Ceria. *Solid State Ionics* **1981**, *2*, 95−105.

(13) Kilner, J. A.; Waters, C. D. The Effects of Dopant Cation-Oxygen Vacancy Complexes on the Anion Transport Properties of Non-stoichiometric Fluorite Oxides. *Solid State Ionics* **1982**, *6*, 253−259.

(14) Yuan, F.; Zhang, Y.; Weber, W. Vacancy-Vacancy Interaction Induced Oxygen Diffusivity Enhancement in Undoped Nonstoichiometric Ceria. *J. Phys. Chem. C* **2015**, *119*, 13153−13159.

(15) Zimicz, M. G.; Lamas, D. G.; Larrondo, S. A. $Ce_{0.9}Zr_{0.1}O_2$ Nanocatalyst: Influence of Synthesis Conditions in the Reducibility and Catalytic Activity. *Catal. Commun.* **2011**, *15*, 68−73.

(16) Zimicz, M. G.; Prado, F. D.; Soldati, A. L.; Lamas, D. G.; Larrondo, S. A. XPD and XANES Studies of $Ce_{0.9}Zr_{0.1}O_2$ Nanocatalysts under Redox and Catalytic CH_4 Oxidation Conditions. *J. Phys. Chem. C* **2015**, *119*, 19210−19217.

(17) Shannon, R. D.; Prewitt, C. T. Effective Ionic Radii in Oxides and Fluorides. *Acta Crystallogr., Sect. B: Struct. Crystallogr. Cryst. Chem.* **1969**, *25*, 925−1048.

(18) Grieshammer, S.; Grope, B. O. H.; Koettgen, J.; Martin, M. A Combined DFT + U and Monte Carlo Study on Rare Earth Doped Ceria. *Phys. Chem. Chem. Phys.* **2014**, *16*, 9974−9986.

(19) Grover, V.; Banerji, A.; Sengupta, P.; Tyagi, A. K. Raman, XRD and Microscopic Investigations on CeO_2-Lu_2O_3 and CeO_2-Sc_2O_3 Systems: A Sub-solidus Phase Evolution Study. *J. Solid State Chem.* **2008**, *181*, 1930−1935.

DOI: 10.1021/acs.jpcc.6b07847
J. Phys. Chem. C 2016, 120, 24165−24175

(20) Moure, A.; Castro, A.; Martínez, I.; Moure, C.; Tartaj, J. Synthesis, Sintering and Ionic Conductivity of Scandia-doped Ceria Ceramic Materials Obtained by Different Procedures. *Ceram. Int.* **2012**, *38*, 5907−5914.
(21) Lee, C. I.; Meng, Q. L.; Kaneko, H.; Tamaura, Y. Solar Hydrogen Productivity of Ceria-scandia Solid Solution using Two-step Water-splitting Cycle. *J. Sol. Energy Eng.* **2013**, *135*, 011002−1.
(22) Burbano, M.; Nadin, S.; Marrocchelli, D.; Salanne, M.; Watson, G. W. Ceria Co-Doping: Synergistic or Average Effect? *Phys. Chem. Chem. Phys.* **2014**, *16*, 8320−5331.
(23) Andersson, D. A.; Simak, S.; Skorodumova, N. V.; Abrikosov, I. A.; Johansson, B. Optimization of Ionic Conductivity in Doped Ceria. *Proc. Natl. Acad. Sci. U. S. A.* **2006**, *103*, 3518−3521.
(24) Burbano, M.; Norberg, S. T.; Hull, S.; Eriksson, S. G.; Marrocchelli, D.; Madden, P. A.; Watson, G. W. Oxygen Vacancy Ordering and the Conductivity Maximum in Y_2O_3-doped CeO_2. *Chem. Mater.* **2012**, *24*, 222−229.
(25) GNOM: Small-angle Scattering Data Processing using the Regularization Technique. Version 4.6, ATSAS team 1991−2009.
(26) Svergun, D. I. Determination of the Regularization Parameter in Indirect-transform Methods using Perceptual Criteria. *J. Appl. Crystallogr.* **1992**, *25*, 495−50.
(27) Rodríguez-Carvajal, J. FULLPROF: a Program for Rietveld Refinement and Pattern Matching Analysis. Satellite Meeting on Powder Diffraction of the XV IUCr Congress, 1990; p 127.
(28) Malet, P.; Caballero, A. The Selection of Experimental Conditions in Temperature-Programmed Reduction Experiments. *J. Chem. Soc., Faraday Trans. 1* **1988**, *84*, 2369.
(29) Ravel, B.; Newville, M. ATHENA, ARTEMIS, HEPHAESTUS: Data Analysis for X-ray Absorption Spectroscopy using IFEFFIT. *J. Synchrotron Radiat.* **2005**, *12*, 537−541.
(30) Thommes, M.; Kaneko, K.; Neimark, A. V.; Olivier, J. P.; Rodriguez-Reinoso, F.; Rouquerol, J.; Sing, K. S. W. Physisorption of Gases, with Special Reference to the Evaluation of Surface Area and Pore Size Distribution (IUPAC Technical Report). *Pure Appl. Chem.* **2015**, *87*, 1051−1069.
(31) Terribile, D.; Trovarelli, A.; Llorca, J.; De Leitenburg, C.; Dolcetti, G. The Preparation of High Surface Area CeO_2-ZrO_2 Mixed Oxides by a Surfactant-assisted Approach. *Catal. Today* **1998**, *43*, 79−88.
(32) Groen, J. C.; Peffer, L. A. A.; Pérez-Ramírez, J. Pore Size Determination in Modified Micro- and Mesoporous Materials. Pitfalls and Limitations in Gas Adsorption Data Analysis. *Microporous Mesoporous Mater.* **2003**, *60*, 1−17.
(33) Fornasiero, P.; Balducci, G.; Di Monte, R.; Kaspar, J.; Sergo, V.; Gubitosa, G.; Ferrero, A.; Graziani, M. Modification of the Redox Behaviour of CeO_2 Induced by Structural Doping with ZrO_2. *J. Catal.* **1996**, *164*, 173−183.
(34) Giordano, F.; Trovarelli, A.; De Leitenburg, C.; Giona, M. A Model for the Temperature-programmed Reduction of Low and High Surface Area Ceria. *J. Catal.* **2000**, *193*, 273−282.
(35) Silversmit, G.; Poelman, H.; Balcaen, V.; Heynderickx, P.; Olea, M.; Nikitenko, S.; Bras, W.; Smet, P.; Poelman, D.; De Gryse, R.; Reniers, M. F.; Marin, G. In-situ XAS Study on the Cu and Ce Local Structural Changes in a CuO-CeO_2/Al_2O_3 Catalyst under Propane Reduction and Re-oxidation. *J. Phys. Chem. Solids* **2009**, *70*, 1274−1284.

DOI: 10.1021/acs.jpcc.6b07847
J. Phys. Chem. C 2016, 120, 24165−24175